

Graphical Model-based Inference on Persistent Homology

Zitian Wu*

Department of Biostatistics, University of Florida
and

Arkaprava Roy†

Department of Biostatistics, University of Florida
and

Leo Duan‡

Department of Statistics, University of Florida

November 19, 2025

Abstract

Persistent homology is a cornerstone of topological data analysis, offering a multi-scale summary of topology with robustness to nuisance transformations, such as rotations and small deformations. Persistent homology has seen broad use across domains such as computer vision and neuroscience. Most statistical treatments, however, use homology primarily as a feature extractor, relying on statistical distance-based tests or simple time-to-event models for inferential tasks. While these approaches can detect global differences, they rarely localize the source of those differences. We address this gap by taking a graphical model-based approach: we associate each vertex with a population latent position in a conic space and model each bar's key events (birth and death times) using an exponential distribution, whose rate is a transformation of the latent positions according to an event occurring on the graph. The low-dimensional bars have simple graph-event representations, such as the formation of a minimum spanning tree or the triangulation of a loop, and thus enjoy tractable likelihoods. Taking a Bayesian approach, we infer latent positions and enable model extensions such as hierarchical models that allow borrowing strength across groups. Applications to a neuroimaging study of Alzheimer's disease demonstrate that our method localizes sources of difference and provides interpretable, model-based analyses of topological structure in complex data.

The code is provided and maintained at <https://github.com/zitian-wu/graphPH>.

Keywords: Competing Exponentials, Latent Position for Persistent Homology, Log-Concave Distribution, Robust Consistency.

*zitianwu@ufl.edu

†arkaprava.roy@ufl.edu

‡li.duan@ufl.edu

1 Introduction

Persistent homology is a foundational tool in topological data analysis that captures topological features of data. Roughly speaking, homology can be thought as k -dimensional holes in a topological space, and persistent homology tracks the birth and death of these holes as a function of a scale parameter. Barcode is commonly used for representing the persistent homology.

To illustrate, we now examine the formation of a barcode via the Vietoris-Rips filtration (Vietoris, 1927; Gromov, 1987), which places a ball of radius ϵ (the scale parameter mentioned above) around each point and gradually increases ϵ . As the radius expands, these balls begin to overlap and merge, connecting nearby points and forming larger connected components, also known as the zero-dimensional (H_0) features. Further, during the growth of ϵ , connected components combine, loops may emerge when multiple connections create cycles. The loop is a one-dimensional (H_1) feature, or intuitively, a one-dimensional hole. Similarly, higher dimensional features/holes could form. By observing how these topological features appear and disappear as ϵ changes, we identify which structures *persist* across multiple scales of ϵ , characterizing the underlying shape and patterns within the data. Figure 1 illustrates such a persistence barcode.

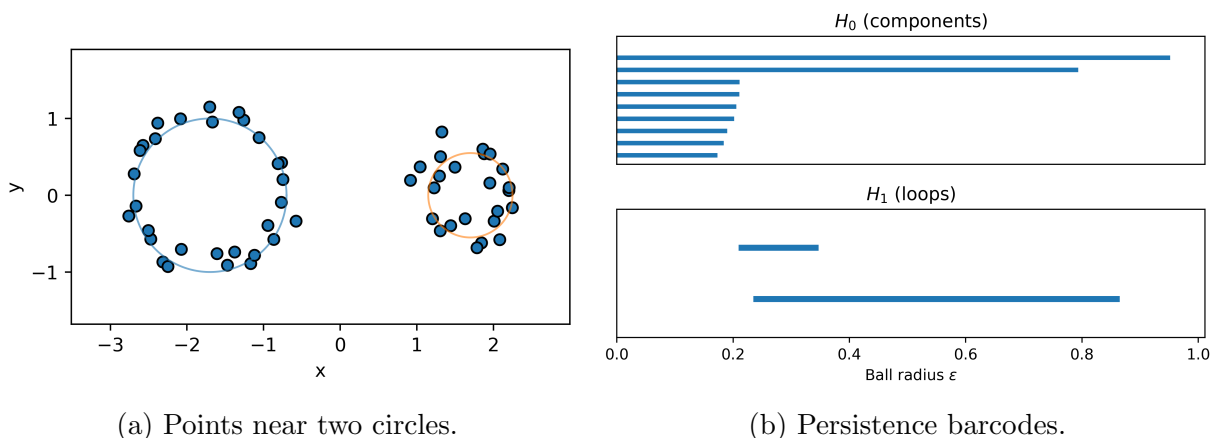


Figure 1: Illustration of the persistent homology of two circles via the Vietoris-Rips filtration: a ball of radius ϵ is placed around each point and is gradually expanded. Zero-dimensional features tracks the formation of connected components, when two components merge, one component persists and the other dies. In this example, although multiple components may form during the expansion, most are short-lived and only two components have a long persistence time (the bars with smaller or infinite death time are omitted). One-dimensional features tracks the formation of two loops, formed when connected components form cycles with holes.

The persistent homology framework is versatile and enjoys a wide variety of filtrations to accommodate different needs for capturing topological features. For example, the Vietoris–Rips captures the relative proximity of points and is invariant under rotation and translation of the data set; the radial sublevel filtration uses the distance from a designated central point, and characterizes radial symmetry or asymmetry.

With an origin in computational topology, persistent homology has gained a surge of

interest in statistical analysis. Progress has been made on quantifying the distribution of features. To be clear on the terminology, one says there is a barcode (a collection of bars) for each subject (such as an image); and over multiple subjects sampled from a population, one obtains a distribution of barcodes. Mileyko et al. (2011) defined probability measures on persistence diagram, a transform of barcode; Cohen-Steiner et al. (2005) showed the stability of diagram, as small perturbations of the sample leads to only small changes in the diagram, hence the diagram enjoys concentration of measure; Fasy et al. (2014) studied bootstrap confidence intervals of persistence diagrams; Moon and Lazar (2023) proposed hypothesis testing procedures on persistence images, a vector representation for diagram (Adams et al., 2017); Bubenik (2015) established that the persistence landscapes (another barcode transform) enjoys appealing large sample properties, such as asymptotic normality of sample mean. Besides these methods, many approaches have been developed for specific applications (Biscio and Møller, 2019; Thomas et al., 2023; Crawford et al., 2020; Moon et al., 2023).

Despite the rich literature, the aforementioned methods are largely based on treating the persistence barcode or its transforms as summary statistics, thereby characterizing the sampling distribution. In parallel, there is a nascent class of model-based approaches in which one imposes a statistical model on the persistence outputs. For example, Maroulas et al. (2020) took a Bayesian approach and modeled the persistence diagrams as Poisson point processes; Garside et al. (2021) considered the barcode as equivalent to survival data, hence allowing for the estimation of the hazard function. Compared to the summary statistic-driven methods, the model-based ones are appealing because they provide model-based smoothing, allow straightforward extensions such as incorporating covariates, and are suitable for inference when the sample size is far from the asymptotic regime.

Our work follows the model-based approach, and is motivated by the goal of *localization*: to identify the source of difference between the barcodes in the original observation space. Clearly, the localization task requires a more fine-grained approach than simply treating the bars as independently generated from a simple distribution (for example, as one would do in a survival model). The key challenge is on how to represent the dependency between the bars in a statistical model.

To achieve the goal of modeling bar dependency, we first note that the homology features are derived from a filtration (a monotonically changing set according to ϵ) of simplicial complex, for which the one-dimensional complex is a graph consisting of vertices and edges, and the two-dimensional complex further involves triangles (binary relationship between three vertices). That means there is already rich information in the simplicial complex. However, a full-scale modeling of the simplicial complex carries a high modeling and computational burden, than focusing on features such as the barcode themselves. For example, for n vertices and T discrete time points, a model that tracks all triangles has an $O(Tn^3)$ computational complexity, which is prohibitive for large n and T .

To address this issue, we propose a middle-ground approach that uses simple graph events to probabilistically represent the key time points of the filtration—the birth and death times of the bars. We show that the zero-dimensional bars can be represented by the formation of a minimum spanning tree, while the one-dimensional bars correspond to the triangulation of a loop. Importantly, we can obtain useful information, such as the edges of the tree and the vertices of the loop, by directly leveraging high-performance computational tools developed by the computational topology community (such as GUDHI, Maria et al.

(2014)), saving statisticians effort to deal with high-dimensional complexes. In this way, one can focus on the low-cost modeling of the remaining graph events. To localize events to specific vertices, we employ a Bayesian latent position model (Hoff et al., 2002) and propose a novel conic space representation that enjoys log-concavity of the posterior distribution, thus ensuring good statistical properties such as identifiability and consistency.

2 Method

To be informative to general statistical readers, we first give a brief introduction to complex filtration, and then describe our graphical model for persistent homology.

2.1 Background on simplicial complex and filtration

Let V be a finite set of points, with each point referred to as a vertex. A *simplicial complex* (or complex for short) \mathcal{K} on V is a collection of finite subsets of V such that: (i) every vertex $v \in V$ appears as a singleton $\{v\} \in \mathcal{K}$; (ii) the set is closed by subsetting, if $\sigma \in \mathcal{K}$ and $\tau \subseteq \sigma$, then $\tau \in \mathcal{K}$. Each member vertex set $\sigma \in \mathcal{K}$ is called a simplex. For example, in a complex $\mathcal{K} = \{\{1\}, \{2\}, \{3\}, \{4\}, \{1, 2\}, \{1, 3\}, \{2, 3\}, \{1, 4\}, \{1, 2, 3\}\}$, each $\sigma \in \mathcal{K}$ is a simplex. We refer to a simplex of size k as a $(k - 1)$ -simplex and may treat it as if it is a fully connected small graph. Thusly, a 0-simplex represents a vertex, a 1-simplex does an edge, a 2-simplex does a triangle, and so on. The nested sequence of complexes $\mathcal{K}_0 \subseteq \mathcal{K}_1 \subseteq \dots \subseteq \mathcal{K}_m$ is called a *filtration* of \mathcal{K}_m .

As discussed above, the standard Vietoris–Rips filtration is constructed from a set of points W equipped with a metric in space, $\text{dist} : \mathcal{Y} \times \mathcal{Y} \rightarrow [0, \infty)$. Given a parameter $\epsilon \geq 0$, a set of $(k + 1)$ points form a k -simplex in \mathcal{K}_ϵ if and only if $\text{dist}(\tilde{y}_j, \tilde{y}_{j'}) \leq \epsilon$ for all $j \neq j'$. We can see that $\mathcal{K}_\infty = \lim_{\epsilon \rightarrow \infty} \mathcal{K}_\epsilon$ can be interpreted as all non-empty subgraphs of a complete graph formed among the data points. Therefore, one may refer to the standard Vietoris–Rips filtration as the Vietoris–Rips filtration of a complete graph. The persistence barcode is a summary statistic of the filtration. We will discuss a few other common filtrations, including Vietoris–Rips filtration of cubical complex, alpha filtration, and sublevel filtration in the supplementary materials. Since most of the filtrations enjoy almost the same graph model-based characterization (except for the sublevel filtration), we focus on the Vietoris–Rips filtration in the main text.

2.2 Persistent homology likelihood

We now take a likelihood-based approach to model the persistent homology outputs. Consider the observed data as \tilde{y}^s with superscript s as the subject index, in some space \mathcal{Y} . We assume the data to be generated from the following likelihood:

$$\tilde{\mathcal{L}}\{\tilde{y}^s \mid (\theta, \rho)\} = \mathcal{G}(\tilde{y}^s \mid y^s; \rho)\mathcal{L}(y^s; \theta), \quad (1)$$

where $y^s = T(\tilde{y}^s)$ is the persistent homology features (such as the barcode and the complexes at birth and death times) generated via a filtration T . We consider θ as the parameter of interest, governing the generative likelihood \mathcal{L} of the features. The change from the features to the observed data is captured by \mathcal{G} , a conditional distribution given y^s , such as those presenting random rotations or small deformations.

In modern statistical and machine learning literature, it has become increasingly easy to model the generative distribution \mathcal{G} , for example by using generative adversarial networks (Goodfellow et al., 2020) with barcode-based distances. Since our primary focus is not on data prediction but on characterizing the between-group differences, we assume the parameters of interest reside only in \mathcal{L} , thus allowing us to ignore \mathcal{G} in our inferential task. We now refer to \mathcal{L} as the persistent homology likelihood, which is a partial likelihood involving $y^{(s)}$ as the sufficient statistic for θ (sufficient under our model assumption). We now introduce some notations.

For ease of notation, we temporarily suppress the index s . Each barcode is a collection of paired time points (b_i^k, d_i^k) , where $b_i^k \geq 0$ is a scalar denoting the birth time, and d_i^k is the death time, $d_i^k \geq b_i^k$ and could take infinite values. For each bar, we augment with a list of edges/edge sets \mathcal{E}_i^k that are directly relevant to the birth/death event. As we show later, \mathcal{E}_i^k can be obtained as some transform of two complexes at the birth and death times. Therefore, our persistent homology features take the following form:

$$y = \{(b_i^k, d_i^k, \mathcal{E}_i^k) : i = 1, \dots, n_k, k = 0, \dots, K\}, \quad (2)$$

and the bar is indexed by $i \in [n_k] = (1, \dots, n_k)$ in each dimension. Following the convention of persistent homology literature, we start counting k from zero, and primarily focus on $k = 0$ and $k = 1$ only in this article. We discuss extensions to higher k in Section 3.2.

Suppose there are n vertices for each subject. We assume the likelihood of all subjects in the same group are dependent on a shared matrix parameter $\Lambda \in (0, \infty)^{n \times n}$ with each element $\lambda_{j,k} = \lambda_{k,j} > 0$. That is, we now consider Λ (or its variants) as the parameter of interest θ from now on. We can now specify the likelihood for the zero-dimensional bars and the one-dimensional bars.

Zero-dimensional bars and minimum spanning tree formation

In the Vietoris-Rips filtration, the zero-dimensional bars represent connected components. We know the number of zero-dimensional bars has $n_0 = n$, and y is a transformation of the pairwise distance matrix $D = \{\Delta_{j,k} : (j, k) \in [n]^2\}$ with $\Delta_{j,k} = \text{dist}(\tilde{y}_j, \tilde{y}_k)$ such as the Euclidean distance. There is an interesting relationship between the zero-dimensional bars and the minimum spanning tree:

$$\hat{T} = \arg \min_{T \in \mathbb{T}} \sum_{(j,k) \in E_T} \Delta_{j,k}$$

where \mathbb{T} is the set of all spanning trees of the complete graph for n vertices, $T = ([n], E_T)$, with E_T containing $n - 1$ edges that connect all n vertices. The connection holds regardless if there are ties in the non-zero distances in D . Nevertheless, for ease of understanding, we will focus on no ties for now.

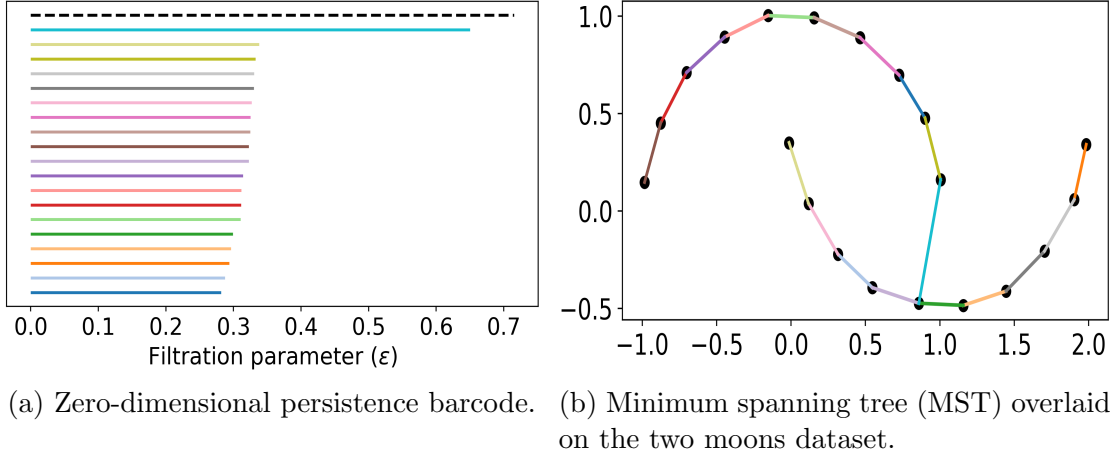


Figure 2: Illustration of using the minimum spanning tree to represent the zero-dimensional bars. Each bar (except for dashed line representing the infinite bar) has a matching edge with same color on the minimum spanning tree.

The minimum spanning tree is uniquely formed (algorithmically determined given D) by the following $(n - 1)$ -step process (Kruskal, 1956). Denoting a forest by \mathcal{F} , as a graph containing disjoint component trees, we index a forest by step t . We start with an \mathcal{F}_1 containing n disjoint trees, each tree having one vertex. From $i = 1$ to $i = n - 1$, we perform the following steps:

- Obtain the admissible edge set

$$A_i = \{ e = (j, k) : j \text{ and } k \text{ are in different components of } \mathcal{F}_i \}.$$

- Add the shortest edge $e_i = \arg \min_{f \in A_i} \Delta_f$, into \mathcal{F}_i , and change notation to \mathcal{F}_{i+1} .

The iterative process terminates at \mathcal{F}_n , which corresponds a single spanning tree.

It is not hard to see that A_i is a monotonically decreasing set, hence the shortest edge e_i is monotonically increasing. Each time an edge is added, a component tree dies due to being merged into another tree — corresponding to the death time of a zero-dimensional bar in persistent homology. Therefore, we have

$$b_i^0 = 0, \quad d_i^0 = \Delta_{(i)}^{\hat{T}}/2,$$

for $i = 1, \dots, n - 1$, where $\Delta_{(i)}^{\hat{T}}$ is the i -th smallest edge length of the minimum spanning tree \hat{T} . Lastly, for $i = n$, $b_n^0 = 0$ and $d_n^0 = \infty$ hence do not need modeling.

In order to represent the above partial ordering relationship, we assign a *competing exponentials model* for the death times of zero-dimensional bar:

$$\begin{aligned} \mathcal{L}[(b_i^0, d_i^0, A_i, e_i)_{i=1}^{n_0}; \Lambda] &= \prod_{i=1}^{n-1} \left[\left(\sum_{f \in A_i} \lambda_f \right) \exp \left(- d_i^0 \sum_{f \in A_i} \lambda_f \right) \frac{\lambda_{e_i}}{\sum_{f \in A_i} \lambda_f} \right] \\ &= \prod_{i=1}^{n-1} \lambda_{e_i} \exp \left(- d_i^0 \sum_{f \in A_i} \lambda_f \right) \end{aligned} \quad (3)$$

where e_i is the i -th edge (with length d_i^0) added to the spanning tree. We use shorthand notation $\lambda_f \equiv \lambda_{j,k}$, as an edge is a pair-index $f = (j, k)$.

In the first line of (3), the exponential density corresponds to length d_i^0 via the first-order statistic transformation of $|A_i|$ -many independent exponential random variables; the next term corresponds to the marginal probability of the edge e_i winning over the other competing edges in A_i . The detailed derivation can be found in Balog et al. (2017).

One-dimensional bars and loop triangulation

The one-dimensional bars correspond to loops. The birth of a loop is when (i) an edge $e_i = (j, k)$ with length b_i^1 forms and is not on the minimum spanning tree \hat{T} , and (ii) there is a path of edges on \hat{T} starting from j and ending at k formed by time b_i^1 . The death happens when the loop is triangulated by the time the last edge $f_i = (j', k')$ with edge length d_i^1 . By triangulation of a loop of m vertices ($m > 3$, as $m = 3$ means immediate triangulation), we mean that at least $(m - 3)$ edges are formed, via which the loop can be divided into non-intersecting triangles. Figure 3 illustrates the loop triangulation event.

There are a few potential complications associated with the loop triangulation: (i) the loop could be triangulated with additional vertex/vertices inside the loop, hence the number of triangulating edges could be more than $(m - 3)$; (ii) one loop could be split into two or more loops at a certain time, hence it is possible that a new loop is born while an existing loop is still alive, leading to edge-dependency between two one-dimensional bars; (iii) by the time a loop dies, there could be more than one set of edges that can triangulate the loop. Although finding the solution of triangulating edges (and the alternative solutions, if not unique) is computationally possible, as to be described in Section 3.2, we propose a lower-bound likelihood modeling all the triangulation-contributing edges for each loop.

To be specific, we compare the two complexes at the birth and death times of a loop, and use the newly added edges connected to the loop vertices. By connected edges, we mean those edges that are directly incident to the loop vertices, or indirectly connected via other vertices. At birth time b_i^1 of a loop, we denote the loop vertices as L_i , and record all the edges of the component graph containing L_i as $E(L_i, b_i^1)$; at the death time d_i^1 , we denote the edges of the component graph containing L_i as $E(L_i, d_i^1)$. We can then see the edges that contribute to the triangulation event except the death edge and those already in the minimum spanning tree, are in $\tilde{B}_i = E(L_i, d_i^1) \setminus E(L_i, b_i^1) \setminus (\{f_i\} \cup E_{\hat{T}})$.

It is not hard to see that forming \tilde{B}_i leads to triangulation, therefore, the probability of forming \tilde{B}_i is smaller or equal to the probability of triangulation. As an edge may contribute to the death of more than one loop, to avoid double counting, we let $B_i = \tilde{B}_i \setminus \bigcup_{j: d_j^1 < d_i^1} \tilde{B}_j$, so it excludes the edges that have already contributed to the death of other loops. Further, note that B_i could include edges that are formed before the loop birth time, we let $B_i = B_i^1 \cup B_i^2$, where B_i^1 corresponds to the edges that are formed during $(0, b_i^1)$, and B_i^2 corresponds to the edges that are formed during (b_i^1, d_i^1) . We assign the following likelihood:

$$\begin{aligned} & \mathcal{L}[(b_i^1, d_i^1, B_i)_{i=1}^{n_1}; \Lambda] \\ &= \prod_{i=1}^{n_1} \left\{ \lambda_{e_i} \lambda_{f_i} \exp(-\lambda_{e_i} b_i^1 - \lambda_{f_i} d_i^1) \prod_{g \in B_i^1} (1 - e^{-\lambda_g b_i^1}) \prod_{h \in B_i^2} (e^{-\lambda_h b_i^1} - e^{-\lambda_h d_i^1}), \right\} \end{aligned} \quad (4)$$

where the first term in the factor is the exponential density for the birth and death times, and the remaining term represents the probabilities for the set containing the other trian-

gulating edges.

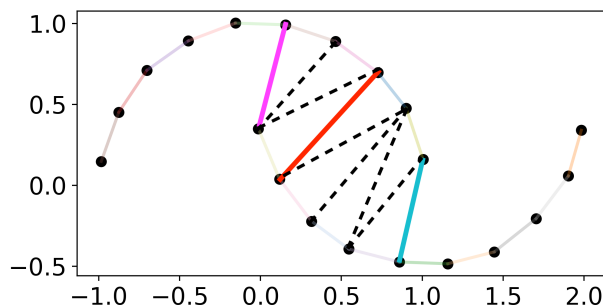


Figure 3: Illustration of the loop triangulation that corresponds to a one-dimensional bar. The magenta edge is associated with the birth of the loop (magenta and the existing edges on the minimum spanning tree, with blue the longest edge on the minimum spanning tree), and the red edge is associated with the loop death. The dashed lines are the triangulation edges with length larger than the birth time and smaller than the death time.

2.3 Bayesian modeling with conic latent coordinates

Since Λ is the matrix that governs the rate of the exponential distribution, we now parameterize it using the latent position model, where each vertex is associated with a latent coordinate z_j in some latent space.

We consider the latent space as a strict acute cone $\mathcal{C} \subset \mathbb{R}^m$ such that

$$z_j^\top z_k > 0 \quad \text{for all } z_j, z_k \in \mathcal{C}.$$

That is, any two vectors in \mathcal{C} have an angle less than 90° . For example, any cone generated by vectors lying in a closed spherical cap of radius at most 45° around some unit vector u , $\text{cone}\{v : \|v\| = 1, v^\top u > \cos(45^\circ)\}$, is an acute cone; the interior of the first quadrant is another acute cone. Although in our model, we do not restrict the orientation of the cone.

We take a Bayesian approach, and assign the following prior for $Z = (z_1, \dots, z_n)$:

$$\pi_0(Z \mid \kappa, \alpha) \propto (\kappa)^{nm/2} \exp\left(-\frac{\kappa}{2} \sum_{j=1}^n \|z_j\|_2^2\right) \prod_{j \leq k} (z_j^\top z_k)^\alpha \quad (5)$$

with $\kappa > 0$, $\alpha > 0$. The exponential kernel regularizes the scale of the latent coordinates, and the product of inner products ensures the positiveness of the inner product of any two latent coordinates. For the latter, its negative logarithmic transform yields $-\alpha \log(z_j^\top z_k)$, which is commonly referred to as the log-barrier function and acts as a strong penalty if the inner product gets too close to 0. We choose a small α to ensure its effect is not pronounced when the inner product is far away from 0. In addition, we include $j = k$ for the benefit of identifiability as described soon.

Since both the likelihood and the prior of Z are invariant to the orthonormal transformation on the rows of Z ($\tilde{Z} = ZP$ for some $P^\top P = I_m$), Z is not directly identifiable in the model. Nevertheless, one may wonder if Z can be identified as an equivariant member in the set $\{Z \in \mathbb{R}^{n \times m} : ZZ^\top = \hat{\Lambda}, m \geq m^0\}$ for some optimal value of $\hat{\Lambda} \succeq 0$ with $\text{rank}(\hat{\Lambda}) = m^0$? We answer affirmatively — in fact, we show that one equivariant posterior mode of Z can be easily found as a second-order stationary point.

Theorem 1. Under the likelihood (3) and (4), and prior (5), consider the conditional posterior of Z given κ and α , reparametrized by $\Lambda = ZZ^\top$, $q_{\kappa,\alpha}(\Lambda) = \Pi(Z \mid \kappa, \alpha, y)$, then the following properties hold:

1. $q_{\kappa,\alpha}(\Lambda)$ is a strictly log-concave function in $\Lambda \succeq 0$ (ignoring the rank constraint), for any finite $\alpha > 0$;
2. The unique maximizer $\hat{\Lambda} = \arg \max q_{\kappa,\alpha}(\Lambda)$ is of rank $m^0 \leq n$ under suitable value of κ .
3. Let $r_{\kappa,\alpha}(Z) = \log \Pi(Z \mid \kappa, \alpha, y)$ with $Z \in \mathbb{R}^{n \times m}$, and each $z_i \in \mathcal{C}$. Suppose given (κ, α) , the rank of $\hat{\Lambda}$ is m^0 , then as long as Z has column dimension $m \geq m^0 + 1$, any Z^* that satisfies the second-order stationarity condition:

$$\nabla r_{\kappa,\alpha}(Z) = 0, \quad \nabla^2 r_{\kappa,\alpha}(Z) \succeq 0$$

has $(Z^*)(Z^*)^\top = \hat{\Lambda}$ and $\text{rank}(Z^*) = m^0$.

Remark 1. We would like to clarify that our focused $q_{\kappa,\alpha}(\Lambda)$ is still the density of Z , except viewed as a function of Λ . The transformed density of Λ would be $q_{\kappa,\alpha}(\Lambda) (\det^* \Lambda)^{\{\text{rank}(Z) - n - 1\}/2}$ (with \det^* pseudo-determinant), which is rank dependent hence not log-concave.

The above equivariant identifiability for Z is not only an encouraging message, but also a principled guide for choosing the dimension of Z in practice: we want to choose m to be sufficiently large, so that it can be *strictly* larger than the rank of the maximizers of $\hat{\Lambda}$ under the a reasonable range in the posterior. The theoretic justification for strict inequality is provided in the proof. This is in line with the common practice in Bayesian modeling of using an overfitted model (Bhattacharya and Dunson, 2011; Van Havre et al., 2015; Legramanti et al., 2020), where one specifies a dimension larger than the expected one and relies on the Bayesian model to shrink the extra dimensions.

In our model, the shrinkage on the rank of the posterior mode is due to $\sum_{j=1}^n \|z_j\|_2^2 = \|\Lambda\|_*$, the nuclear norm commonly used in optimization to induce low-rank optimal solution. Since we use a continuous prior for Z , the posterior Λ has rank m almost everywhere, but is concentrated near $\hat{\Lambda}$ with rank m^0 . We use prior $\kappa \sim \text{Ga}(2, 3)$ so it has prior mean 6, while the prior support κ vanishes at 0. We set $m = 5$ for the column dimension of Z , and $\alpha = 0.1$ in the positive barrier term. Empirically, these values lead to good mixing performance for the Markov chains.

2.4 Hierarchical model for multi-group data analysis

We next extend our model to accommodate multiple subjects drawn from several groups, indexed by $p = 1, \dots, P$. For the S_p subjects belonging to the p -th group, each subject $s \in \mathcal{I}_p$ is associated with its own barcode and edge set, denoted y^s . Assuming that the data $\{y^s : s \in \mathcal{I}_p\}$ are conditionally independent, the likelihood can be expressed as

$$\mathcal{L}(\{y^s : s \in \mathcal{I}_p\}; \Lambda^p) = \prod_{s \in \mathcal{I}_p} \mathcal{L}[(b_t^{[s]0}, d_t^{[s]0}, A_t^{[s]0})_{t=1}^{n_0^{[s]}}; \Lambda^p] \mathcal{L}[(b_t^{[s]1}, d_t^{[s]1}, B_t^{[s]1})_{t=1}^{n_1^{[s]}}; \Lambda^p].$$

For different groups, we assign each with an individual Λ^p .

For statistical modeling, it is very useful to borrow strength across groups, so that we can shrink the Λ^p toward a common $\bar{\Lambda}$, while having the significant differences that remain show the source of the across-group variability. For this goal, we develop a Bayesian hierarchical prior for modeling a collection $\{\Lambda^1, \dots, \Lambda^P\}$ based on the Procrustes-type distance that minimizes the negative impact of free orthonormal transformation on the difference between Λ^p and $\bar{\Lambda}$.

Consider a latent matrix $\bar{Z} \in \mathbb{R}^{n \times m} \cap \mathcal{C}^n$ with m sufficiently large, we define the distance squared between $Z^p : Z^p Z^{p\top} = \Lambda^p$ and $\bar{Z} : \bar{Z} \bar{Z}^\top = \bar{\Lambda}$ as

$$\text{dist}^2(Z^p, \bar{Z}) = \min_{R^\top R=I, s \in \mathbb{R}} \|Z^p - s\bar{Z}R\|_F^2 = \|Z^p\|_F^2 - \|Z^{p\top} \bar{Z}\|_*^2 / \|\bar{Z}\|_F^2$$

where R represents any orthonormal transform, and s does any scaling. The second equality is due to the fact that the closed-form solution for the minimizer: $\hat{R} = UV^\top$, with $UDV^\top = \bar{Z}^\top Z^p$ the singular value decomposition, and $\hat{s} = \text{tr}(Z^{p\top} \bar{Z} \hat{R}) / \|\bar{Z}\|_F^2 = \|Z^{p\top} \bar{Z}\|_* / \|\bar{Z}\|_F^2$, with $\|\cdot\|_*$ the nuclear norm.

Since $\|Z^{p\top} \bar{Z}\|_* = \text{tr}((\bar{Z}^\top \Lambda^p \bar{Z})^{1/2})$, and $\|Z^p\|_F^2 = \text{tr}(\Lambda^p)$, we have the following hierarchical prior that extends (5):

$$\begin{aligned} \Pi_0(Z^p | \bar{Z}) &\propto (\kappa)^{nm/2} \exp\left(-\frac{\kappa}{2} \left[\|\bar{Z}\|_F^2 \text{tr}(\Lambda^p) - [\text{tr}((\bar{Z}^\top \Lambda^p \bar{Z})^{1/2})]^2 \right]\right) \prod_{j \leq k} (z_j^{p\top} z_k^p)^\alpha \\ &\quad \text{for } p = 1, \dots, P, \\ \Pi_0(\bar{Z}) &\propto \exp\left(-\frac{1}{2} \kappa_0 \|\bar{Z}\|_F^2\right) \prod_{j \leq k} (\bar{z}_j^\top \bar{z}_k)^\alpha, \end{aligned}$$

in which $\Pi_0(Z^p | \bar{Z})$ is again a strictly log-concave function in $\Lambda_p \succeq 0$. Since the Procrustes-type distance is invariant to the scaling of \bar{Z} , we fix $\kappa_0 = 6$ in the prior for \bar{Z} .

3 Posterior Computation

We now discuss the posterior computation for our proposed model. One may notice that in our likelihood, the edge sets are not directly known from the barcode, hence need to be calculated from the data. Fortunately, these sets only need to be pre-computed once for each subject s , and are invariant to the value of the parameters; given the edge sets, the posterior computation can be carried out efficiently. We now first discuss the posterior sampling algorithm, then discuss the algorithm for finding the edges.

3.1 Markov chain Monte Carlo with warm-start

We use the No-U-Turn Sampler (NUTS, Hoffman and Gelman (2014)) to estimate the posterior distribution. For the implementation, we use the numpyro package (Bingham et al., 2019) for its low implementation cost of the proposed model using the automatic differentiation capabilities. Due to the popularity of No-U-Turn Sampler algorithms in the Bayesian literature and the high level of automation provided by software packages, we refer the reader to Hoffman and Gelman (2014) for the details. Here we provide a brief summary of the algorithm, and use the remaining space to discuss a few key aspects specific to our approach.

The No-U-Turn Sampler algorithm is a variant of the Hamiltonian Monte Carlo algorithm, which uses discretized approximation of Hamiltonian dynamics to propose new samples. The Hamiltonian dynamics describe the evolution of a system in terms of position \tilde{q} (equivalent to our parameter θ) and momentum \tilde{p} (an equal-dimensional vector of auxiliary variables) by

$$\frac{d\tilde{q}}{dt} = \nabla_{\tilde{p}} H, \quad \frac{d\tilde{p}}{dt} = -\nabla_{\tilde{q}} H,$$

where $H(\tilde{q}, \tilde{p})$ is the Hamiltonian energy function of the system, as the sum of the negative log-posterior (except for the constant term) and augmented kinetic energy for \tilde{q} , typically of form $\tilde{q}^\top \tilde{M} \tilde{q}$ with \tilde{M} a positive definite matrix. The No-U-Turn Sampler algorithm extends Hamiltonian Monte Carlo by adaptively determining the trajectory length, automatically stopping the simulation when the path begins to double back, which avoids the need to manually tune path lengths and improves exploration of the posterior distribution.

There are two points specific to our proposed model. First, on handling the acute cone constraint on the matrix Z , thanks to the $F(Z) = -\alpha \sum_{i \leq j} \log(z_i^\top z_j)$ term in the negative log-prior, we see that the gradient of the log-prior with respect to Z

$$\nabla_Z F(Z) = -\alpha C Z, \quad C_{jj} = \frac{2}{\lambda_{jj}}, \quad C_{jk} = \frac{1}{\lambda_{jk}} \quad (j \neq k).$$

Therefore, the momentum change direction in $-\nabla_{\tilde{q}} H$ contains

$$-\{\nabla_Z F(Z)\}_j = \alpha \left(\frac{2}{\lambda_{jj}} z_j + \sum_{k \neq j} \frac{1}{\lambda_{jk}} z_k \right).$$

If $\lambda_{jj} = \|z_j\|^2 \downarrow 0$, the term $(2/\lambda_{jj}) z_j$ will explode along z_j , making $z_j^\top z_j$ larger and away from zero. Similarly, if an off-diagonal $\lambda_{jk} = z_j^\top z_k \downarrow 0$, the term $(1/\lambda_{jk}) z_k$ will explode along z_k (and symmetrically for z_k along z_j), aligning the two rows hence making $z_j^\top z_k$ more positive and further away from zero. Although the discretization error of the Hamiltonian dynamics may create $z_j^\top z_k < 0$, the Metropolis-Hastings step rejects the proposal. Therefore, provided the initial value of Z is in the acute cone, the algorithm can efficiently maintain the constraint in the subsequent iterations.

Second, we can exploit the conditional log-concavity of the posterior distribution to warm-start the No-U-Turn Sampler. The warm-start strategy has two major benefits: first, it reduces the time for burn-in, and; second, it improves the stability of the algorithm as the automatic tuning of the algorithm (such as choosing the step size) is carried out in the high posterior density region. Specifically, fixing $\kappa = 6$ (prior mean), we first run gradient ascent (with $\Lambda = ZZ^\top$ parameterized) to find a conditional mode \hat{Z} of the posterior distribution, then use \hat{Z} and $\kappa = 6$ as the initial value for the Markov chain. We find the strategy empirically effective in inducing fast convergence and good mixing performance.

3.2 Finding simplices associated with birth and death events

We now describe useful algorithms for finding the simplices (such as edges and triangles) important for the birth and death of bars. To be general, we introduce the boundary matrix-based algorithm that is nearly universally applicable to all persistent homology features, including two- or higher-dimensional ones.

For ease of understanding, we focus on the simplex where the edge orientation does not matter. At time t , the boundary matrix ∂_k^t has the rows corresponding to all the $(k-1)$ -simplices, and the columns corresponding to all the k -simplices:

$$(\partial_k^t)_{\sigma^{k-1}, \tau^k} = \begin{cases} 1 & \text{if } \sigma^{k-1} \text{ is a face of } \tau^k, \\ 0 & \text{otherwise.} \end{cases}$$

in which, face means a nonempty vertex set. For example, vertex σ^0 is a face of edge τ^1 if the edge is incident to the vertex, and ∂_1 is the vertex-edge incidence matrix of the graph at time t ; edge τ^1 is a face of triangle τ^2 if the triangle is incident to the edge, and ∂_2 is the edge-triangle incidence matrix at time t . The boundary matrix is useful as it allows us to identify the simplices using linear algebra modulo 2.

To illustrate, we now focus on the birth and death events of a loop. First, to identify the edges (among $|E_t|$ many edges) that form a new loop at a birth time t due to the newly added edge τ_t , we use the matrix ∂_1^t , and the edges correspond to the ones in the binary vector $x \in \{0, 1\}^{|E_t|}$:

$$\partial_1^t x \equiv 0 \pmod{2} \quad \text{and} \quad x_{\tau_t} = 1,$$

where $\equiv 0 \pmod{2}$ means equal 0 after the modulo 2 operation. Solving the system can be done using Gaussian elimination modulo 2, which replaces subtraction with XOR operation.

Second, to identify the triangles that fill the loop (formed earlier at a birth time t' , with the edges denoted by $x^{t'}$) due the newly added triangle τ_t at a death time t , we can use matrix ∂_2^t and we know the triangles corresponding to ones in the binary vector y :

$$\partial_2^t y \equiv x^{t'} \pmod{2} \quad \text{and} \quad y_{\tau_t} = 1.$$

To clarify, the solution may not be unique, and some solutions may use more triangles than a minimal filling, which we refer to as triangulation in a previous section and can be found by simply taking the solution(s) with the least number of triangles.

The above two computational strategies are easy to implement, and importantly, directly extensible for higher-dimensional simplices. For example, at the birth of a void (two-dimensional feature) at time t , the list of triangles can be found via the solution of $\partial_2^t x \equiv 0 \pmod{2}$ and $x_{\tau_t} = 1$. For the death of a void (filled by tetrahedra) when τ_t is added, the list of tetrahedra can be found via the solution of $\partial_3^t y \equiv x^{t'} \pmod{2}$ and $y_{\tau_t} = 1$.

With the great generality of the linear algebra modulo 2 solution, the Gaussian elimination associated with a $k_1 \times k_2$ matrix has a cost of $\mathcal{O}(\min(k_1 k_2^2, k_2 k_1^2))$. Therefore, application of the above algebraic solutions may have an expensive cubic cost. On the other hand, the cost can be tolerable, since the calculation is only needed once for each subject, before running Markov chain Monte Carlo. In the supplementary materials, we also discuss some alternative solutions that are specific to our proposed model, hence less general but with much lower cost.

4 Asymptotic theory for persistent homology posterior

In this section, we study the asymptotic behavior of the posterior distribution under the persistent homology model. We establish the asymptotic result under two related but different settings. First, we focus on the ideal case where the model is correctly specified,

and potentially, a diverging number of zero-dimensional features are collected. This setting allows us to obtain not only the consistency of the model parameters, but also the convergence rate of the posterior distribution. Second, we then generalize and consider the case where the persistent homology may contain higher-dimensional features, but the model could be misspecified to some extent. We establish a set of sufficient conditions for the consistent recovery of feature membership, an important characteristic of the topology, and discuss possible extensions on how to ensure the robust consistency result hold.

4.1 Consistency and convergence rate under correct model specification

In this section, we establish the consistency of estimating the model parameters Λ , and characterize the convergence rate of the posterior distribution to the true parameter Λ_0 . Clearly, this implies the true generating law is included in our specified family of models. For the purpose of rate characterization, we focus on the case where the zero-dimensional features are collected, for which we know that there are always $(n - 1)$ zero-dimensional features. We can rewrite the joint likelihood based on (3) as

$$\prod_{s=1}^S \prod_{i=1}^{n-1} \lambda_{e_i^{[s]}} \exp \left(- \sum_{f \in E} \lambda_f \sum_{i: f \in A_i^{[s]0}} d_i^{[s]0} \right)$$

where E is the set of all edges. Assuming m is chosen to be sufficiently large, we now assume the following conditions:

- (C1) The parameter space of Z is bounded, such that $\lambda_{j,k} \in [a, b]$ for all j, k for some positive constants a, b away from zero and infinity, where $\lambda_{j,k} = z_j^\top z_k$.
- (C2) For all $f \in E$, $\mathbb{E}_0(\sum_{i: f \in A_i^0} d_i^0) = O(n)$ and is bounded away from zero, where \mathbb{E}_0 is the expectation under the true law.

In the above, (C1) guarantees that Λ is also bounded, which we use to show convergence in the Frobenius norm for Λ . In the absence of (C1), posterior consistency holds with respect to the total variation distance. (C2) is a mild condition on the expectation that ensures the proper large sample behavior. With the above, we establish the large support for the proposed prior on Z .

Lemma 1 (Large Support for the prior of Z). *For Z drawn from the prior (5), for any $Z_* \in \mathbb{R}^{n \times m} : \|Z_*\|_\infty < C_z$, some constant $C_z > 0$, and any $\epsilon > 0$, there exists $\delta(n) > 0$ such that the prior probability*

$$\Pi(\|Z - Z_*\|_F < \epsilon) > \delta(n),$$

further, we have $\Pi(\|Z\|_F > R_\epsilon) \leq \epsilon$ with $R_\epsilon^2 = \frac{1}{\kappa} (\nu - 2 + 2 \log \frac{C'}{\epsilon})$.

We provide the detail of $\delta(n)$ in the proof.

Since the likelihood only depends on the off-diagonal elements of Λ , we now consider Λ_0 as a symmetric matrix with zero diagonal elements, and we define $\text{LTri}(\Lambda)$ as the vectorized lower triangular part of matrix Λ . We denote the sequence of posterior distributions of Λ by $\Pi_S(\cdot | Y_S)$, while allowing n to be fixed or potentially growing with S .

Theorem 2 (Posterior consistency for Λ). *Under the assumptions (C1) and (C2), for every fixed ϵ ,*

$$\mathbb{E}_0 \Pi_S(\|\text{LTri}(\Lambda - \Lambda_0)\|_2^2 > M_S \epsilon_S \mid Y_S) \rightarrow 0$$

as $S \rightarrow \infty$ with $\epsilon_S = \sqrt{n \log S / S}$ for any $M_S \rightarrow \infty$.

The above rate characterization is an encouraging result showing that as long as $S/\{\log(S)M_S\}$ grows slightly faster than the number of vertices, we will be able to recover the true parameter Λ_0 . One may take any diverging M_S , such as $M_S = (\log S)^{0.1}$.

4.2 Consistent recovery of the topological feature-membership under some model misspecification

Next, we consider a general setting where the features can have dimension greater or equal to one, and the true generating law of the homology may fall outside our specified class of models. Due to the possibility of model misspecification, we do not hope to recover the true generating law of the homology exactly, but we still want to correctly quantify some aspects of the topology. In particular, we focus on the feature-membership, defined as if a vertex belongs to a certain topological feature, such as in the formation of a loop.

To formalize the quantity of interest under the ground truth, for each subject s , let $D^{(s)} = \{\Delta_{j,k}^{(s)}\}_{j < k}$ be the subject's distance matrix, and we assume the data-generating distribution $D^{(s)} \stackrel{iid}{\sim} F^0$, where F^0 is some unknown distribution. We define the subject-level indicator vector

$$\iota^{(s)} = g(D^{(s)}) \in \{0, 1\}^{|V|}$$

where g returns which vertices form a certain topological feature. Across S subjects, we know that $\hat{p}_S(v) = \frac{1}{S} \sum_{s=1}^S \iota_v^{(s)} \rightarrow p_{F^0}(v) = \mathbb{P}_{F^0}(\iota_v = 1)$ as $S \rightarrow \infty$ by the law of large numbers.

On the other hand, under our specified model parameterized by Λ . Let Q_Λ be the model-implied law of D from which we can simulate new distance. We have a model-induced distribution $\mathbb{P}_{Q_\Lambda}(\iota_v = 1)$ for the feature-membership. A natural question is when can we have $\mathbb{P}_{Q_\Lambda}(\iota_v = 1) \rightarrow p_{F^0}(v)$ as the posterior distribution of Λ concentrates? The following theorem provides a set of sufficient conditions.

Theorem 3. *Let E be a finite index set of distances and let \mathcal{C} be a finite collection of rank relations on E . Let $\Omega_{\mathcal{C}}$ denote the finite set of partial orderings induced by \mathcal{C} , and let $R : \text{Perm}(E) \rightarrow \Omega_{\mathcal{C}}$ be the restriction map. There exists a subset $\mathcal{A}_v \subseteq \Omega_{\mathcal{C}}$ such that $\iota_v = \mathbf{1}\{R \in \mathcal{A}_v\}$ almost surely, hence under F^0 , ι_v is a random event determined by $R \in \Omega_{\mathcal{C}}$. If the following conditions hold:*

(C3) *For any D , there exists a neighborhood $C_D = \{D' : g(D') = g(D)\} \ni D$ with $\text{radius}(C_D) \geq \delta_0 > 0$, and under the true law F^0 ties occur with probability 0.*

(C4) *The feature $\iota_v = g(D)$ is determined solely by the relative ordering among $\{\Delta_{i,j}\}_{i < j}$.*

(C5) *There exist weights $\eta \in (0, \infty)^{|E|}$ such that the full ranking of $\{\Delta_e\}_{e \in E}$ under F^0 follows the Plackett–Luce law $\text{PL}(\eta)$; equivalently, for any permutation π of E ,*

$$\mathbb{P}_{F^0}(\Delta_{\pi(1)} < \cdots < \Delta_{\pi(|E|)}) = \prod_{k=1}^{|E|} \frac{\eta_{\pi(k)}}{\sum_{\ell \geq k} \eta_{\pi(\ell)}}.$$

(C6) There is a continuous map $\Lambda \mapsto \theta(\Lambda) \in (0, \infty)^E$ such that the model-implied law of R is

$$p_{\bar{\theta}(\Lambda)}^{\mathcal{C}} = R[\text{PL}(\bar{\theta}(\Lambda))] \quad \text{on } \Omega_{\mathcal{C}}, \quad \bar{\theta}(\Lambda) = \theta(\Lambda) / \sum_{e \in E} \theta_e(\Lambda).$$

The restricted family $\bar{\theta} \mapsto p_{\bar{\theta}}^{\mathcal{C}}$ is identifiable on the simplex $\Delta^{|E|-1}$.

(C7) The prior for Λ on the symmetric matrix space \mathbb{S}^n is absolutely continuous w.r.t. Lebesgue measure and has a strictly positive density on every nonempty open set.

(C8) The following Kullback-Leibler divergence is minimized at some $\Lambda : \theta(\Lambda) = c\eta$ for some constant $c > 0$:

$$\text{KL}(F^0 \parallel Q_{\Lambda}) = \text{KL}(F_R^0 \parallel Q_R(\cdot; \bar{\theta}(\Lambda))) + \mathbb{E}_{F_R^0} \left[\text{KL}(F_{M|R}^0 \parallel Q_{M|R}(\cdot \mid R; \Lambda)) \right],$$

where M denotes the lengths of bars in the barcode.

Let $\hat{\Lambda}_S$ be a draw from the posterior based on S i.i.d. observations of R . Then, for every v ,

$$\mathbb{P}_{Q_{\hat{\Lambda}_S}}(\iota_v = 1) \xrightarrow[S \rightarrow \infty]{P} p_{F^0}(v) := \mathbb{P}_{F^0}(\iota_v = 1).$$

Our consistency of partial information recovery is inspired by the results established for the rank likelihood framework (Hoff et al., 2014). Most of the above conditions are considered standard in the literature, except for (C3) and (C6). Condition (C3) constrains the true law of the partial orderings to a family. Despite being a restriction, the Plackett–Luce family is routinely used in the literature (Guiver and Snelson, 2009; Caron and Teh, 2012). Condition (C6) assumes that the misspecified model on the barcode lengths does not impact the recovery of the ranking law. To make (C6) more generally applicable, one could extend our model by first treating b_i^k and d_i^k as noisy realization near latent β_i^k and δ_i^k , and using the competing exponential-based likelihood of β_i^k and δ_i^k using the observed partial ordering.

5 Simulation studies

We conduct simulation studies to evaluate the performance of our method. We first generate three group oracles (sets of points in \mathbb{R}^2) that are related to each other: in Group 1, we draw $\mu_i^{(1)} \sim N(0, 0.25^2 I)$ for $i = 1, \dots, 150$; in Group 2, we have $\mu_i^{(2)} = \mu_i^{(1)}$ for $i = 1, \dots, 75$, while $\mu_i^{(2)} \sim N(\Delta 1, 0.25^2 I)$ for $i = 76, \dots, 150$, with $\Delta > 0$ a scalar; in Group 3, we have $\mu_i^{(3)} = \mu_i^{(1)}$ for $i = 1, \dots, 45$, $\mu_i^{(3)} \sim N(\Delta 1, 0.25^2 I)$ for $i = 46, \dots, 75$, and $\mu_i^{(3)} = \mu_i^{(2)}$ for $i = 76, \dots, 150$. Effectively at the oracle, Group 1 and Group 2 are 50% different, Group 2 and Group 3 are 40% different, and Group 1 and Group 3 are 70% different. Then in each group, we add independent Gaussian noise from $N(0, 0.07^2 I)$ to each point in the oracle, and obtain the data points \tilde{y}_i^s . We simulate 10 subjects in each group, and conduct repeated experiments under three different values of $\Delta \in \{0.5, 1, 2\}$.

Figure 4 shows the persistence barcode for one subject in each group under $\Delta = 1$. We can see clear differences between Group 1 and the other two, but the differences between Groups 2 and 3 are not obvious since they differ only in the proportion of points near locations 0 and $\Delta 1$.

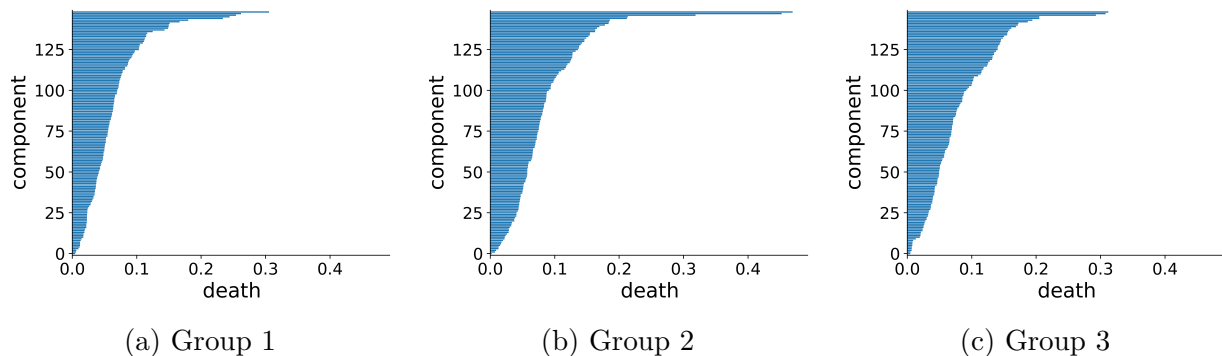


Figure 4: Zero-dimensional persistence barcodes for vertices generated near (a, Group 1) one point in \mathbb{R}^2 , (b, Group 2 and c, Group 3) near two points separated by vector $(\Delta 1)$ in \mathbb{R}^2 . Group 1 has bar death times much smaller than those in Group 2 and Group 3. On the other hand, the difference between Groups 2 and 3 are not obvious in the barcode, since the two groups differ only in the proportion of points near the two points.

We fit our model to the simulated data and estimate the posterior. In each setting, we run 1000 iterations of the sampler, with the first 500 iterations discarded as burn-in. For visualizing the latent coordinates, we first calculate the posterior mean of $\hat{\Lambda}^p$ for $p = 1, 2, 3$ (under $m = 5$), then obtain a low rank approximate decomposition of $\hat{\Lambda}^p \approx (\tilde{Z}^p \tilde{Z}^p)^T$ using truncated SVD at rank 2. We apply $O(2)$ orthonormal transformations, so that the distances $\|\tilde{Z}^1 - \tilde{Z}^2\|_F$ and $\|\tilde{Z}^2 - \tilde{Z}^3\|_F$ are minimized.

Figure 5 plots the coordinates \tilde{Z}_i^p in the three groups. Clearly, the latent coordinates in Group 1 are close to each other, while those in Group 2 and Group 3 have a two-cluster structure (colored in yellow and blue). Comparing the latent coordinates in Group 2 and Group 3, we can see that there are 30 vertices (colored in red) that are mixed with the blue cluster under Group 2, whereas the vertices of the same indices are mixed with the yellow cluster under Group 3. The result is the effect of localization on which vertices contribute to the difference between the two groups.

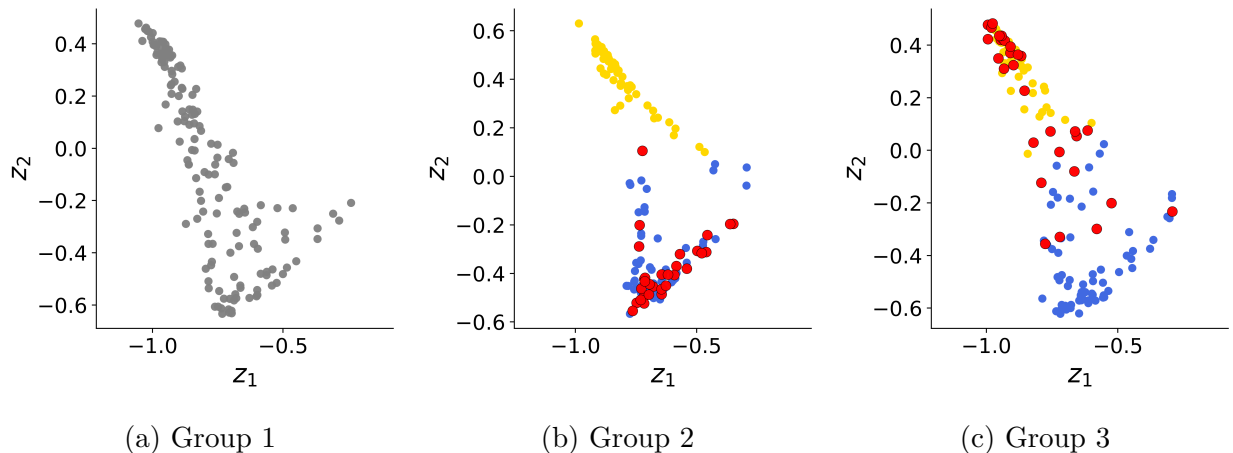


Figure 5: Visualization of estimated latent coordinates in two dimensions. The difference between Groups 2 and 3 can now be localized to the 30 vertices (colored in red) that are mixed in the cluster 1 (blue) under Group 2, whereas the vertices of the same indices are mixed in the cluster 2 (yellow) under Group 3.

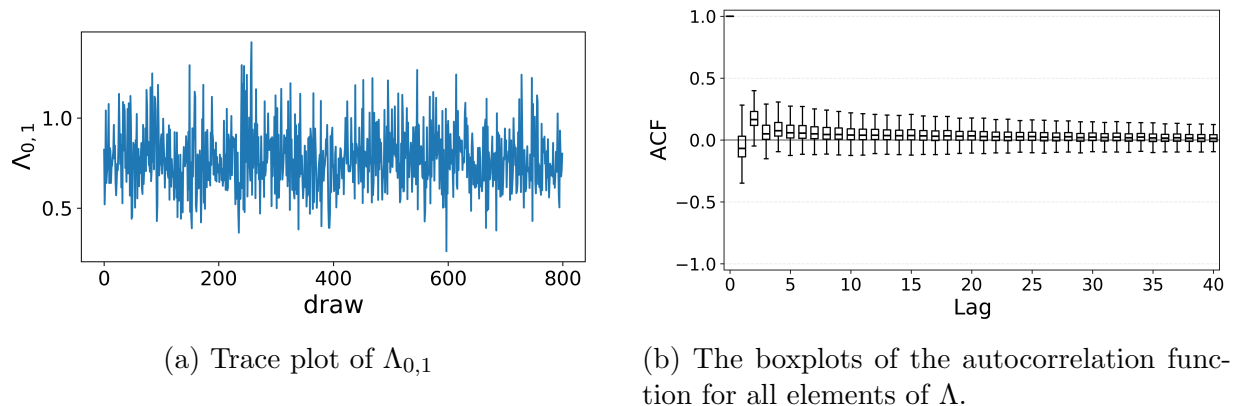


Figure 6: Markov chain diagnostics shows that the posterior distribution can be efficiently sampled by the No-U-Turn Sampler.

The No-U-Turn Sampler shows excellent mixing of Markov chains and the autocorrelation function decays rapidly to near zero. Figure 6 shows the trace plot of one element of Λ , and the boxplot of the autocorrelation function for all elements of Λ , under $\Delta = 1$. We find similar results under $\Delta = 0.5$ and $\Delta = 2$. In addition, we conduct experiments where the data are generated near two circles of different radii, hence producing both zero-dimensional and one-dimensional features. We provide the details in the supplementary materials.

6 Data application

We now apply our method to analyze the structural connectivity data related to Alzheimer’s disease. Alzheimer’s disease (AD) is a major neurodegenerative disorder, with early detection of brain changes considered essential for effective treatment. A key research focus is how white matter changes as the disease progresses (Phillips et al., 2015). Studies show

that structural connectivity alterations spread with disease progression (Tucholka et al., 2018) and tend to impact reduced connectivity brain regions (Daianu et al., 2016). White matter changes are also linked to amyloid plaque buildup, a hallmark of Alzheimer’s disease that emerges before clinical symptoms (Prescott et al., 2014). Most prior work relies on scalar connectivity metrics derived from brain imaging, but these can be sensitive to how the metric is defined (Phillips et al., 2015). In this study, we use data from the Alzheimer’s Disease Neuroimaging Initiative (ADNI), which provides connectome information for $n = 83$ brain regions. For each region pair, both the count and mean length of connecting white matter fibers are available. There are $S = 102$ subjects in the dataset, consisting of three groups: cognitively normal (CN) with 26 subjects, mildly cognitively impaired (MCI) with 46 subjects and Alzheimer’s disease (AD) with 37 subjects.

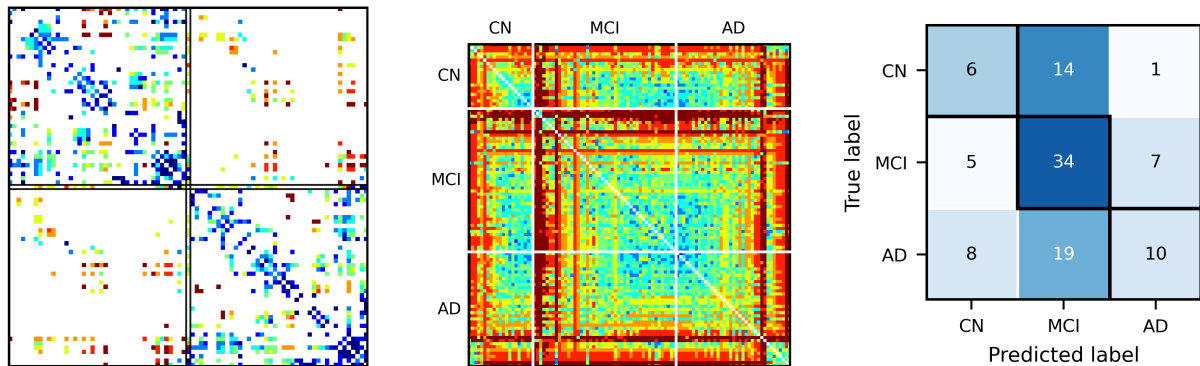


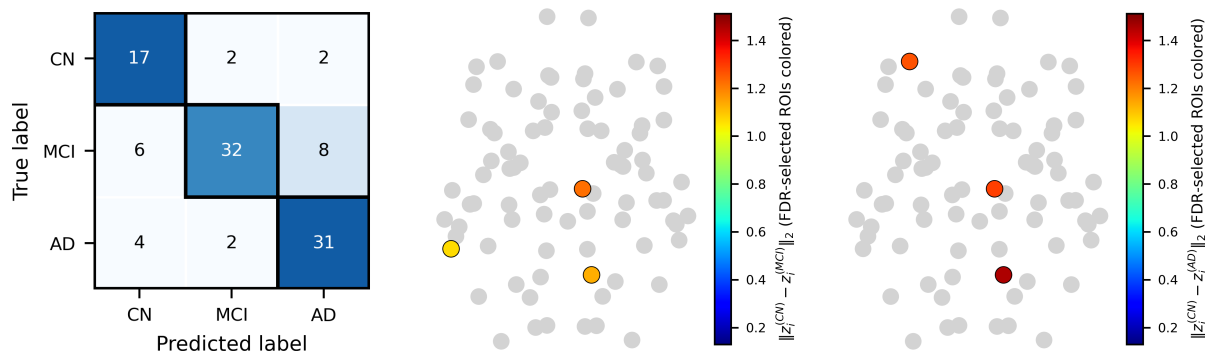
Figure 7: Exploratory analysis using the bottleneck distance.

The structural connectomes are pre-processed according to the pipeline in Roy et al. (2019), each subject connectivity score matrix is symmetric and consists of $n(n - 1)/2$ entries, with each score greater than or equal to 0 and represents the strength of the connection between the two regions. We apply a spectral embedding via Laplacian eigenmaps to convert the connectivity scores to distances, then apply the Vietoris–Rips filtration to obtain the persistent homology.

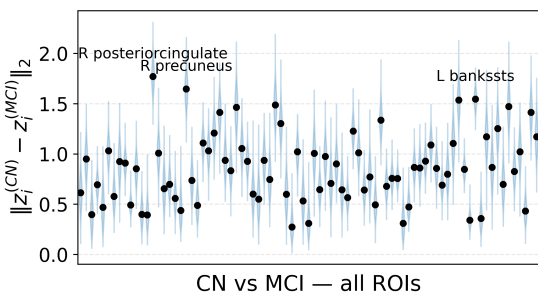
In the exploratory analysis, we first compute the bottleneck distance between the persistence diagrams of all the subjects, and plot the distance matrix in Figure 7(b). The subjects are arranged according their group label, however, we can hardly see any group pattern in the bottleneck distance matrix. In order to quantitatively assess the difference between the groups, we fit a K -nearest neighbor classifier to the data, and report the prediction accuracy in confusion matrix 7(c), corresponding to the prediction accuracy of 3-class classifier only at 48.1%, and the one between normal (CN) and diseased (MCI and AD combined) at 73.1%.

With the existing scientific finding that established across-group differences in the structural connectivity, the lack of group-discriminative patterns in the bottleneck distance matrix is somewhat surprising. This clearly suggests that useful signals are likely distorted in

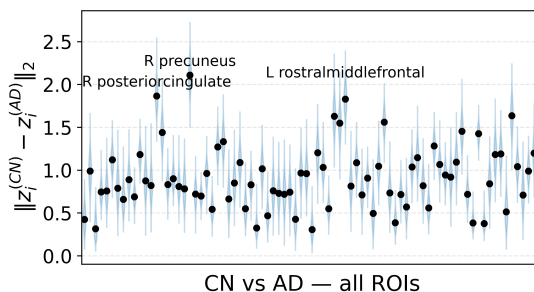
the calculation of the bottleneck distance (as a global metric comparing two homologies) hence motivating localizing approach.



(a) Persistence homology likelihood model show much lower misclassification rate in the confusion matrix, compared to the classifier based on the raw connectivity scores. (b) Dorsal view of the brain regions of interest with significant differences between the cognitive normal and mildly cognitively impaired groups. (c) Dorsal view of the brain regions of interest with significant differences between the cognitive normal and Alzheimer’s disease groups.



(d) Violin plot showing the posterior distribution of the distance between the latent coordinates of the regions, between the cognitive normal and mildly cognitively impaired groups.



(e) Violin plot showing the posterior distribution of the distance between the latent coordinates of the regions, between the cognitive normal and Alzheimer’s disease groups.

Figure 8: The persistent homology model using hierarchical prior shows good discriminability between the three groups, and allows us to localize the source of the difference down to a few regions.

We fit our model to the data and estimate the posterior. We use optimization-based warm start to find the conditional mode of the posterior distribution, then run 10000 iterations of the sampler, with the first 500 iterations discarded as burn-in. Using the posterior mean of the parameter $\tilde{\Lambda}^p$, we use the maximum likelihood classifier $\hat{c}_i = \arg \max_{c \in \{1,2,3\}} \hat{p}(y^s | \tilde{\Lambda}^p)$ to predict the group assignment for each subject. We see a clear improvement in the prediction accuracy compared to the K -nearest neighbor classifier, with the prediction accuracy of 3-class classifier reaching 76.9%, and the one between normal and diseased reaching 86.5%.

For comparison, we also fit a 3-class logistic regression model with lasso regularization

on the raw connectivity scores, and a 3-class ordinal regression model with 5-fold cross-validation. The prediction accuracy of the logistic regression model is 43.3% (78.8% for normal and diseased), and the one of the ordinal regression model is 48.1% (78.8% for normal and diseased). We can see that our proposed method achieves much better performance than the two baseline models.

We now localize the source of the difference down to a few regions. We first calculate the pairwise distance between the latent coordinates of the regions, $\|z_i^{(p)} - z_i^{(p')}\|_2$ in each posterior sample, then we plot the posterior distribution of the coordinate-wise distance in Figure 8(d,e). Then we follow the Bayesian false discovery rate (FDR) control approach in (Müller et al., 2007; Kiran Chandra et al., 2021) to identify the regions with significant differences between the groups. At false discovery rate level less or equal to 0.1, we identify 3 regions with significant differences between the cognitive normal and mildly cognitively impaired groups, and 3 regions with significant differences between the cognitive normal and Alzheimer’s disease groups. Figure 8(b)(c) highlight the regions corresponding to major differences.

7 Discussion

In this article, we propose a likelihood-based approach that models the birth and death events of persistent homology features in terms of corresponding graph events. The introduction of latent coordinate for the vertices in the simplicial complex allows us to localize the between-group differences, while quantify the uncertainty for statistical inference. There are a few interesting directions that can be pursued in the future. First, since one could simultaneously obtain more than one type of filtrations (such as the sublevel filtration from different radial centers) from the data, there is a need for filtration selection based on the level of informativeness. Extending our hierarchical model-based approach, one could consider a group shrinkage prior that jointly shrinking group-specific latent coordinates toward some commonality while allowing heterogeneity. There is a large literature in hierarchical, multiscale, or structural shrinkage models (Guhaniyogi and Sanso, 2020; Kundu and Lukemire, 2024; Boss et al., 2024) that can be adapted to our setting. Second, one could extend our approach to multi-parameter persistent homology (Botnan and Lesnick, 2022), under which the complex may evolve under several simultaneous scales. Although the birth and death events must be defined differently, which requires some modifications to the order-based likelihood representations discussed above, the core idea can be applied: we can use relatively simple graph events to capture the key changes occurring in the potentially high-dimensional simplicial complex, enabling feasible statistical estimation and inference.

References

- Adams, H., T. Emerson, M. Kirby, R. Neville, C. Peterson, P. Shipman, S. Chepushtanova, E. Hanson, F. Motta, and L. Ziegelmeier (2017). Persistence images: A stable vector representation of persistent homology. *Journal of Machine Learning Research* 18(8), 1–35.

- Balog, M., N. Tripuraneni, Z. Ghahramani, and A. Weller (2017). Lost relatives of the Gumbel trick. In *International Conference on Machine Learning*, pp. 371–379. PMLR.
- Bhattacharya, A. and D. B. Dunson (2011). Sparse Bayesian infinite factor models. *Biometrika* 98(2), 291–306.
- Bingham, E., J. P. Chen, M. Jankowiak, F. Obermeyer, N. Pradhan, T. Karaletsos, R. Singh, P. A. Szerlip, P. Horsfall, and N. D. Goodman (2019). Pyro: Deep universal probabilistic programming. *Journal of Machine Learning Research* 20, 1–6.
- Biscio, C. A. and J. Møller (2019). The accumulated persistence function, a new useful functional summary statistic for topological data analysis, with a view to brain artery trees and spatial point process applications. *Journal of Computational and Graphical Statistics* 28(3), 671–681.
- Boss, J., J. Datta, X. Wang, S. K. Park, J. Kang, and B. Mukherjee (2024). Group inverse-gamma gamma shrinkage for sparse linear models with block-correlated regressors. *Bayesian Analysis* 19(3), 785–814.
- Botnan, M. B. and M. Lesnick (2022). An introduction to multiparameter persistence. *arXiv preprint arXiv:2203.14289* 2(5).
- Bubenik, P. (2015). Statistical topological data analysis using persistence landscapes. *Journal of Machine Learning Research* 16(1), 77–102.
- Burer, S. and R. D. Monteiro (2005). Local minima and convergence in low-rank semidefinite programming. *Mathematical programming* 103(3), 427–444.
- Caron, F. and Y. Teh (2012). Bayesian nonparametric models for ranked data. *Advances in Neural Information Processing Systems* 25.
- Cohen-Steiner, D., H. Edelsbrunner, and J. Harer (2005). Stability of persistence diagrams. In *Proceedings of the Twenty-first Annual Symposium on Computational Geometry*, pp. 263–271.
- Crawford, L., A. Monod, A. X. Chen, S. Mukherjee, and R. Rabadán (2020). Predicting clinical outcomes in glioblastoma: an application of topological and functional data analysis. *Journal of the American Statistical Association* 115(531), 1139–1150.
- Daianu, M., M. F. Mendez, V. G. Baboyan, Y. Jin, R. J. Melrose, E. E. Jimenez, and P. M. Thompson (2016). An advanced white matter tract analysis in frontotemporal dementia and early-onset Alzheimer’s disease. *Brain Imaging and Behavior* 10(4), 1038–1053.
- Edelsbrunner, H. and G. Osang (2023). A simple algorithm for higher-order delaunay mosaics and alpha shapes. *Algorithmica* 85(1), 277–295.
- Fasy, B. T., F. Lecci, A. Rinaldo, L. Wasserman, S. Balakrishnan, and A. Singh (2014). Confidence sets for persistence diagrams. *The Annals of Statistics* 42(6), 2301–2339.
- Garside, K., A. Gjoka, R. Henderson, H. Johnson, and I. Makarenko (2021). Event history and topological data analysis. *Biometrika* 108(4), 757–773.

- Ghosal, S. and A. van der Vaart (2007). Convergence rates of posterior distributions for non-iid observations. *The Annals of Statistics*, 192–223.
- Ghosal, S. and A. van der Vaart (2017). *Fundamentals of Nonparametric Bayesian Inference*. Cambridge University Press, Cambridge.
- Goodfellow, I., J. Pouget-Abadie, M. Mirza, B. Xu, D. Warde-Farley, S. Ozair, A. Courville, and Y. Bengio (2020). Generative adversarial networks. *Communications of the ACM* 63(11), 139–144.
- Gromov, M. (1987). Hyperbolic groups. In *Essays in group theory*, pp. 75–263. Springer.
- Guhaniyogi, R. and B. Sanso (2020). Large multi-scale spatial modeling using tree shrinkage priors. *Statistica Sinica* 30(4), 2023–2050.
- Guiver, J. and E. Snelson (2009). Bayesian inference for Plackett-Luce ranking models. In *Proceedings of the 26th Annual International Conference on Machine Learning*, pp. 377–384.
- Hoff, P. D., X. Niu, and J. A. Wellner (2014). Information bounds for Gaussian copulas. *Bernoulli* 20(2), 604.
- Hoff, P. D., A. E. Raftery, and M. S. Handcock (2002). Latent space approaches to social network analysis. *Journal of the American Statistical Association* 97(460), 1090–1098.
- Hoffman, M. D. and A. Gelman (2014). The No-U-Turn sampler: adaptively setting path lengths in Hamiltonian Monte Carlo. *Journal of Machine Learning Research* 15(1), 1593–1623.
- Kiran Chandra, N., P. Müller, and A. Sarkar (2021). Bayesian scalable precision factor analysis for massive sparse Gaussian graphical models. *arXiv preprint arXiv:2107.11316*.
- Kruskal, J. B. (1956). On the shortest spanning subtree of a graph and the traveling salesman problem. *Proceedings of the American Mathematical Society* 7(1), 48–50.
- Kundu, S. and J. Lukemire (2024). Flexible Bayesian product mixture models for vector autoregressions. *Journal of Machine Learning Research* 25(146), 1–52.
- Legramanti, S., D. Durante, and D. B. Dunson (2020). Bayesian cumulative shrinkage for infinite factorizations. *Biometrika* 107(3), 745–752.
- Maria, C., J.-D. Boissonnat, M. Glisse, and M. Yvinec (2014). The GUDHI library: Simplicial complexes and persistent homology. In *International Congress on Mathematical Software*, pp. 167–174. Springer.
- Maroulas, V., F. Nasrin, and C. Oballe (2020). A Bayesian framework for persistent homology. *SIAM Journal on Mathematics of Data Science* 2(1), 48–74.
- Mileyko, Y., S. Mukherjee, and J. Harer (2011). Probability measures on the space of persistence diagrams. *Inverse Problems* 27(12), 124007.

- Moon, C. and N. A. Lazar (2023). Hypothesis testing for shapes using vectorized persistence diagrams. *Journal of the Royal Statistical Society Series C: Applied Statistics* 72(3), 628–648.
- Moon, C., Q. Li, and G. Xiao (2023). Using persistent homology topological features to characterize medical images: Case studies on lung and brain cancers. *The Annals of Applied Statistics* 17(3), 2192–2211.
- Müller, P., G. Parmigiani, and K. Rice (2007). FDR and Bayesian multiple comparisons rules. *Bayesian Statistics 8: Proceedings of the Eighth Valencia International Meeting June 2–6, 2006* 8.
- Phillips, D. J., A. McGlaughlin, D. Ruth, L. R. Jager, A. Soldan, and Alzheimer’s Disease Neuroimaging Initiative (2015). Graph theoretic analysis of structural connectivity across the spectrum of Alzheimer’s disease: The importance of graph creation methods. *NeuroImage: Clinical* 7, 377–390.
- Prescott, J. W., A. Guidon, P. M. Doraiswamy, K. Roy Choudhury, C. Liu, J. R. Petrella, and A. D. N. Initiative (2014). The Alzheimer’s structural connectome: changes in cortical network topology with increased amyloid plaque burden. *Radiology* 273(1), 175–184.
- Roy, A., S. Ghosal, J. Prescott, and K. R. Choudhury (2019). Bayesian modeling of the structural connectome for studying Alzheimer’s disease. *The Annals of Applied Statistics* 13(3), 1791–1816.
- Thomas, A. M., P. A. Crozier, Y. Xu, and D. S. Matteson (2023). Feature detection and hypothesis testing for extremely noisy nanoparticle images using topological data analysis. *Technometrics* 65(4), 590–603.
- Tucholka, A., O. Grau-Rivera, C. Falcon, L. Rami, R. Sanchez-Valle, A. Llado, J. D. Gisbert, J. L. Molinuevo, and A. D. N. Initiative (2018). Structural connectivity alterations along the Alzheimer’s disease continuum: reproducibility across two independent samples and correlation with cerebrospinal fluid amyloid- β and tau. *Journal of Alzheimer’s Disease* 61(4), 1575–1587.
- Van Havre, Z., N. White, J. Rousseau, and K. Mengersen (2015). Overfitting Bayesian mixture models with an unknown number of components. *PloS one* 10(7), e0131739.
- Vietoris, L. (1927). Über den höheren Zusammenhang kompakter Räume und eine Klasse von zusammenhangstreuen Abbildungen. *Mathematische Annalen* 97(1), 454–472.

A Supplementary Materials

A.1 Extension to Other Filtrations

Generalized Vietoris–Rips Filtration

Naturally, we do not have to force \mathcal{K}_∞ to correspond to a complete graph, potentially leading to more interpretable filtrations in practice. For example, in image data analysis, it is common to have \mathcal{K}_∞ as a cubical complex, where the largest simplex has each vertex only connected to its neighboring vertices in the spatial grid. In this case, we can define a Vietoris–Rips filtration of a cubical complex, $\mathcal{K}_\epsilon = \text{VRC}(W, \epsilon)$, such that each σ has $\text{dist}(w_i, w_j) \leq \epsilon$ and (i, j) are neighbors in the spatial grid, for all pairs $(i, j) \in \sigma$.

With the potentially different choice of \mathcal{K}_∞ , we can see the graph-event representations developed above are still valid, except that there would be fewer edges in the admissible sets for forming spanning tree or triangulation, compared to the complete graph case.

Alpha Filtration

We now extend to other type of filtrations. First, we consider the alpha filtration on Delaunay complex: $\text{Delaunay}(W) = \mathcal{K}_\infty = \{\sigma \subseteq V : \cap_{i \in \sigma} \mathcal{V}(w_i) \neq \emptyset\}$, where $\mathcal{V}(w_i) = \{w \in \mathcal{Y} : \text{dist}(w, w_i) \leq \text{dist}(w, w_j) \text{ for all } w_j \in V\}$ is commonly called the Voronoi cell of w_i . The alpha filtration is then formed with a ball $B(w_i, \epsilon) = \{w \in \mathcal{Y} : \text{dist}(w, w_i) \leq \epsilon\}$.

$$\text{Alpha}(W, \epsilon) = \mathcal{K}_\epsilon = \{\sigma \subseteq V : \cap_{i \in \sigma} [\mathcal{V}(w_i) \cap B(w_i, \epsilon)] \neq \emptyset\}.$$

Further, one may consider a weighted version of the alpha filtration Edelsbrunner and Osang (2023), where the distance is replaced by a power distance function (which is not a metric): $\text{power-dist}(w, w_i) = \|w - w_i\|^2 - \nu_i$, with $\nu_i \geq 0$ an assigned weight associated with the point w_i . We can immediately see a connection to the Vietoris–Rips filtration of the Delaunay complex: it is the exactly the same as the unweighted alpha filtration, and equivalent to the weighted alpha filtration after replacing the metric by the power distance function. Hence again, the graph-event representations developed above are directly applicable to the alpha filtrations.

Sublevel Filtration

Next, we consider the sublevel filtration (or lower-star filtration, as in some literature). Given a function $\phi : \mathcal{Y} \rightarrow \mathbb{R}$, the canonical definition of sublevel filtration for the set W is

$$\text{Sublevel}(W, \epsilon) = \mathcal{K}_\epsilon = \{\sigma \subseteq V : \phi(w_i) \leq \epsilon \text{ for all } i \in \sigma\}.$$

Hence \mathcal{K}_∞ is the power set of V minus the empty set. For ϕ , one could consider some score function such as a probability density estimate (kernel density filtration), or the distance to a reference point (radial filtration).

Unlike the previously discussed filtrations, this definition of sublevel filtration lacks a graph interpretation. Fortunately, when it comes to computing persistent homology features (such as connected components and loops), one does consider an auxilliray graph $H_\epsilon = (V, E_H(\epsilon))$, with $(i, j) \in E_H(\epsilon)$ only if (i) there is an edge $(i, j) \in E_G$ on another underlying graph G that is predefined and invariant to ϵ (such as the cubical grid graph), and (ii) $i, j \in \sigma$ for some $\sigma \in \mathcal{K}_\epsilon$.

We can see it is more convenient to a vertex-centric distribution to model the bars in the sublevel filtration. We again use an exponential distribution with vertex-wise rate λ_i .

Clearly, some modifications are needed for the sublevel filtration. For simplicity, we assume $\phi(w_i) > 0$ for all $w_i \in W$ and no ties in $\phi(w_i)$. First of all, each vertex i could become a zero-dimensional bar with a positive birth time $\phi(w_i)$, with a positive length if $\phi(w_i) < \phi(w_j)$ for all the adjacent vertices $j : (i, j) \in E_G$. That is w_i corresponds to a strict local minimum of ϕ on the graph G . To find out the death time, we again

consider a minimum spanning tree \hat{T} , formed via the Kruskal procedure except with $\Delta_{j,k} = \max[\phi(w_j), \phi(w_k)]$. Then the death time for the zero-dimensional bar is associated with the addition of a vertex j that simultaneously connects to the tree component containing i and to an earlier component. That is, $\phi(w_j) > \phi(w_k)$ for all k in the earlier component and the component(s) that just died — equivalently, as we observe $d_0^i = \phi(w_j)$ for some j , k is simply all the other vertices in the same component as j at time d_0^i .

On the other hand, the one-dimension bars for the sublevel filtration are similar to those of the Vietoris–Rips filtration. The birth time is associated with the formation of a loop, and the death time is associated with the fill-in of a loop, except using vertices instead of edges.

B Proof of the Theorems

B.1 Proof of Theorem 1

Proof. For (i), we first note the log-likelihood of Λ as

$$\begin{aligned} \log \mathcal{L}(y; \Lambda) = & \text{const} + \sum_{k=0}^K \left\{ \sum_{e \in \mathcal{E}_{1,k}} \log \lambda_e - \sum_{e \in \mathcal{E}_{2,k}} \alpha_{e,k} \lambda_e \right. \\ & \left. + \sum_{e \in \mathcal{E}_{3,k}} \log(1 - e^{-\lambda_e \beta_{e,k}}) + \sum_{e \in \mathcal{E}_{4,k}} \log(e^{-\lambda_e \beta_{e,k}} - e^{-\lambda_e \gamma_{e,k}}) \right\}, \end{aligned}$$

with $\mathcal{E}_{i,k}$, $i = 1, 2, 3, 4$, the appropriate sets of edges, and $\alpha_{e,k}$, $\beta_{e,k}$, $\gamma_{e,k}$ the birth and death times, and c a constant. It is not hard to see that the log-likelihood is a concave function in λ_e .

The log-prior is equivalent to

$$\log \pi_0(Z \mid \kappa, \alpha) = \text{const} - \frac{\kappa}{2} \sum_{i=1}^n \Lambda_{i,i} + \alpha \sum_{i \leq j} \log(\Lambda_{i,j})$$

in which, the sum of logarithmic function is strictly concave when $\alpha > 0$, and covers all elements of $\Lambda_{i,j}$. Therefore, the log-posterior is a strictly log-concave function in $\Lambda \succeq 0$.

For (ii), note that when $\Lambda \succeq 0$, $\sum_{i=1}^n \Lambda_{i,i} = \|\Lambda\|_*$, the nuclear norm of Λ . Therefore, $(\kappa/2)$ can be viewed the Lagrange multiplier for the nuclear norm constraint $\|\Lambda\|_* \leq r_{m^0}$, hence by strong duality of a concave function, there exists a suitable value of κ , for the maximizer $\hat{\Lambda}$ to be of rank m^0 .

For (iii), we note that $-r_{\kappa,\alpha}(Z)$ is twice differentiable in $Z \in \mathbb{R}^{n \times m} \cap \mathcal{C}^n$. Burer and Monteiro (2005) shows that for any convex and twice differentiable problem of positive semi-definite matrix Λ with $\text{rank}(\Lambda) = m^0$, the solution of the second-order stationary point under reparametrization by $\Lambda = ZZ^\top$, with $Z \in \mathbb{R}^{n \times m}$ has $(Z^*)(Z^*)^\top = \hat{\Lambda}$, provided $m > m^0$ strictly. \square

B.2 Proof of Lemma 1

Proof. Let $Z = [z_1, \dots, z_n] \in \mathbb{R}^{m \times n}$ with support $\{z_j^\top z_k \geq 0\}$ and density

$$\pi(Z) \propto \exp\left(-\frac{\kappa}{2}\|Z\|_F^2\right) \prod_{j \leq k} (z_j^\top z_k)^\alpha, \quad \kappa > 0, \alpha > 0.$$

Let $R = \|Z\|_F$ and set $\nu = mn + \alpha n(n-1)$.

Applying Cauchy–Schwarz, we have for each j, k , $(z_j^\top z_k)^\alpha \leq (\|z_j\| \|z_k\|)^\alpha$, hence

$$\prod_{j \leq k} (z_j^\top z_k)^\alpha \leq \prod_{j=1}^n \|z_j\|^{\alpha(n-1)}.$$

Applying AM-GM inequality at fixed R , we have $\sum_{j=1}^n \|z_j\|^2 = R^2$, and the product is maximized when $\|z_j\| = R/\sqrt{n}$, so

$$\prod_{j=1}^n \|z_j\|^{\alpha(n-1)} \leq \left(\frac{R}{\sqrt{n}}\right)^{\alpha n(n-1)}.$$

Viewing Z as a vector in \mathbb{R}^{mn} , $dZ = R^{mn-1} dR d\sigma$, so for some finite constant C ,

$$\Pr(R \geq r) \leq C \int_r^\infty s^{mn-1+\alpha n(n+1)} e^{-\kappa s^2/2} ds = C' e^{-\kappa r^2/2} \left(\frac{\kappa r^2}{2}\right)^{\frac{\nu}{2}-1}.$$

Set

$$R_\varepsilon^2 = \frac{1}{\kappa} \left(\nu - 2 + 2 \log \frac{C'}{\varepsilon} \right),$$

which ensures $\Pr(\|Z\|_F > R_\varepsilon) \leq \varepsilon$. Thus the Frobenius ball $\mathcal{S}_\varepsilon = \{Z : \|Z\|_F \leq R_\varepsilon\}$ is a $(1 - \varepsilon)$ large-support set, with $R_\varepsilon \asymp \sqrt{\nu/\kappa}$, where \asymp stands for asymptotic equivalence.

By continuity of the map $Z \mapsto z_j^\top z_k$, there exists $\varepsilon_0 > 0$ such that $\|Z - Z_*\|_F < \varepsilon_0$, thus $z_j^\top z_k \geq \frac{\tau}{2}$ for all $j \leq k$. Hence, for all such Z , $\prod_{j \leq k} (z_j^\top z_k)^\alpha \geq \left(\frac{\tau}{2}\right)^{\alpha M}$, $M = \frac{n(n-1)}{2}$, and $\exp\left(-\frac{\kappa}{2}\|Z\|_F^2\right) \geq \exp\left(-\frac{\kappa}{2}(\|Z_*\|_F + \varepsilon_0)^2\right)$. Therefore the density is bounded below by a positive constant on the ball $B_F(Z_*, \varepsilon_0) = \{Z : \|Z - Z_*\|_F < \varepsilon_0\} = \frac{\pi^{mn/2}}{\Gamma(\frac{mn}{2}+1)} \varepsilon_0^{mn}$.

Thus $\pi(Z) \geq c_0 = \frac{1}{Z_\pi} \exp\left(-\frac{\kappa}{2}(\|Z_*\|_F + \varepsilon_0)^2\right) \left(\frac{\tau}{2}\right)^{\alpha M} > 0$, where Z_π is the (finite) normalizing constant. Hence, for any $\varepsilon \in (0, \varepsilon_0]$, $\Pi(\|Z - Z_*\|_F < \varepsilon) \geq c_0 \text{Vol}(B_F(Z_*, \varepsilon)) = \delta(n) > 0$. \square

B.3 Proof of Theorem 2

Proof. To derive the posterior contraction rate ϵ_S asserted in Theorem 2, we apply the general theory of posterior contraction from Section 8.3 of Ghosal and van der Vaart (2017). This requires verifying certain that prior concentration in a ball of size ϵ_S^2 in the sense of Kullback-Leibler divergence, existence of tests with error probabilities at most $e^{-c_1 S \epsilon_S^2}$ for testing the true distribution against a ball of size of the order ϵ_S separated by more

than ϵ_S from the truth in terms of the metric d_S , a *sieve* in the parameter space which contains at least $1 - e^{-c_2 n \epsilon_S^2}$ prior probability and which can be covered by at most $e^{c_3 n \epsilon_S^2}$ for some constants $c_1, c_3 > 0$ and $c_2 > c_1 + 2$. By direct calculation and Taylor series expansion, along with the finiteness of the first-order raw moment of d_i^0 under $\Lambda_{0,s}$, we have $\frac{1}{S} KL(f_{\Lambda_1}, f_{\Lambda_0}) \lesssim n \|\Lambda_1 - \Lambda_0\|_F \lesssim n \|Z_1 - Z_0\|_F$. Applying the support result from Lemma 1, we have $-\log(\Pi(\|Z_1 - Z_0\|_F < \frac{\epsilon_S}{n})) \lesssim n \log S$, assuming the rate ϵ_S cannot be faster than parametric convergence rate of $S^{-1/2}$ and $S > n$. Equating this with $S \epsilon_S^2$ gives us the pre-rate of $\sqrt{\frac{n \log S}{S}}$.

By Lemma 2 of Ghosal and van der Vaart (2007), exponentially consistent tests exists with respect to the Hellinger and thus for the total variation distance as well. Due to assumed boundedness of the support, the *sieve* condition is automatically satisfied. This proves the posterior consistency under the total variation distance with rate same as the pre-rate $\sqrt{\frac{n \log S}{S}}$. Specifically we have the posterior probability of the ball $\{f_{\Lambda_1} : \int |f_{\Lambda_1}(y) - f_{\Lambda_0}(y)| dy < \epsilon\}$ around f_{Λ_0} goes to 1 almost surely. Note that $\int |f_{\Lambda_1}(y) - f_{\Lambda_0}(y)| dy = \mathbb{E}_{y \sim f_{\Lambda_0}} |1 - \frac{f_{\Lambda_1}(y)}{f_{\Lambda_0}(y)}|$. Assuming the support of Λ bounded, we have

$$C_1 \exp\left(-\sum_f (\lambda_f - \lambda_{0,f}) \sum_s \sum_{i:f \in A_i} y_i^0\right) < \frac{f_{\Lambda_1}(y)}{f_{\Lambda_0}(y)} < C_2 \exp\left(-\sum_f (\lambda_f - \lambda_{0,f}) \sum_s \sum_{i:f \in A_i} y_i^0\right).$$

Then using the result that $\log(1 - \epsilon) \leq \epsilon$ for ϵ close to zero and finiteness of $\mathbb{E}(y_i^0)$, we have the posterior probability of $\{\Lambda : |\Lambda - \Lambda_0|_F^2 \lesssim \epsilon\}$ goes 1. Results from Ghosal and van der Vaart (2007) can be utilized to establish equivalent results for the more general multi-group multi-subject case in Section 2.4. \square

B.4 Proof of Theorem 3

Proof. Let $\bar{\eta} = \eta / \sum_{e \in E} \eta_e$. By (iii) and the restriction map R , the true law of the restricted ordering is $p_{\bar{\eta}}^c := R[\text{PL}(\bar{\eta})]$ on the finite set Ω_C . By (iv), the model induces $p_{\bar{\theta}(\Lambda)}^c = R[\text{PL}(\bar{\theta}(\Lambda))]$.

Because Ω_C is finite, the map $\bar{\theta} \mapsto p_{\bar{\theta}}^c$ is continuous, and by (iv) the parameterization is identifiable on the simplex. By (v) there exists Λ^\dagger with positive prior support and $\bar{\theta}(\Lambda^\dagger) = \bar{\eta}$. Since the posterior for Λ concentrates in probability on the set of KL minimizers, for every neighborhood U of $\bar{\eta}$, $\Pi(\bar{\theta}(\Lambda) \in U \mid R_{1:S}) \xrightarrow{P}_{S \rightarrow \infty} 1$. Consequently, for any posterior draw $\hat{\Lambda}_S$, $\left\| p_{\bar{\theta}(\hat{\Lambda}_S)}^c - p_{\bar{\eta}}^c \right\|_{\text{TV}} \xrightarrow{P}_{S \rightarrow \infty} 0$. Since $\iota_v = \mathbf{1}\{R \in \mathcal{A}_v\}$ almost surely, $\mathbb{P}_{Q_{\hat{\Lambda}_S}}(\iota_v = 1) = \sum_{r \in \mathcal{A}_v} p_{\bar{\theta}(\hat{\Lambda}_S)}^c(r)$, $p_{F^0}(v) = \sum_{r \in \mathcal{A}_v} p_{\bar{\eta}}^c(r)$. Thus

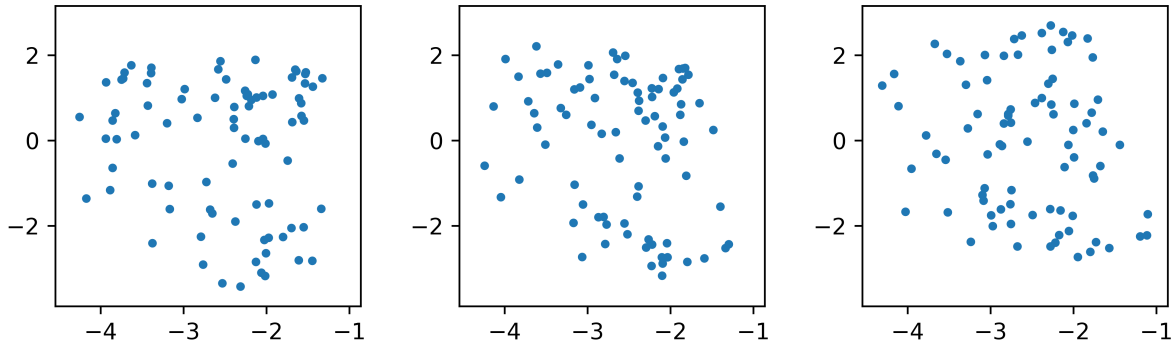
$$\begin{aligned} \left| \mathbb{P}_{Q_{\hat{\Lambda}_S}}(\iota_v = 1) - p_{F^0}(v) \right| &= \left| \sum_{r \in \mathcal{A}_v} (p_{\bar{\theta}(\hat{\Lambda}_S)}^c(r) - p_{\bar{\eta}}^c(r)) \right| \\ &\leq \sum_{r \in \Omega_C} |p_{\bar{\theta}(\hat{\Lambda}_S)}^c(r) - p_{\bar{\eta}}^c(r)| \\ &= 2 \left\| p_{\bar{\theta}(\hat{\Lambda}_S)}^c - p_{\bar{\eta}}^c \right\|_{\text{TV}}, \end{aligned}$$

which converges to 0 in probability. \square

B.5 Alternative edge-finding algorithms specific to the proposed model

In our implementation, we can take shortcut that bypasses the need for Gaussian elimination. Since we start with the persistence barcode generated by the high-performance persistent homology software GHUDI (Maria et al., 2014), the additional cost of finding the edges is low. For the zero-dimensional bars, the spanning tree edges have been sorted according to the lengths, hence we further find the admissible edges via simple thresholding with an $\mathcal{O}(n_0)$ cost using vectorized matrix operation. For the one-dimensional bars, we find the edge set by taking the set differences of two connected components. Since the connected components are given in the homology software output, the additional edge-finding cost for each one-dimensional bar is close to constant, leading to a total cost $\mathcal{O}(n_1)$.

B.6 Additional details for the data application



(a) Latent positions for the cognitively normal group (b) Latent positions for the mildly cognitively impaired group (c) Latent positions for the Alzheimer's disease group

Figure 9: Visualization of the latent positions for the three groups in two dimensions. The posterior mean of Λ is first calculated, then a low rank approximation is obtained using truncated SVD at rank 2.

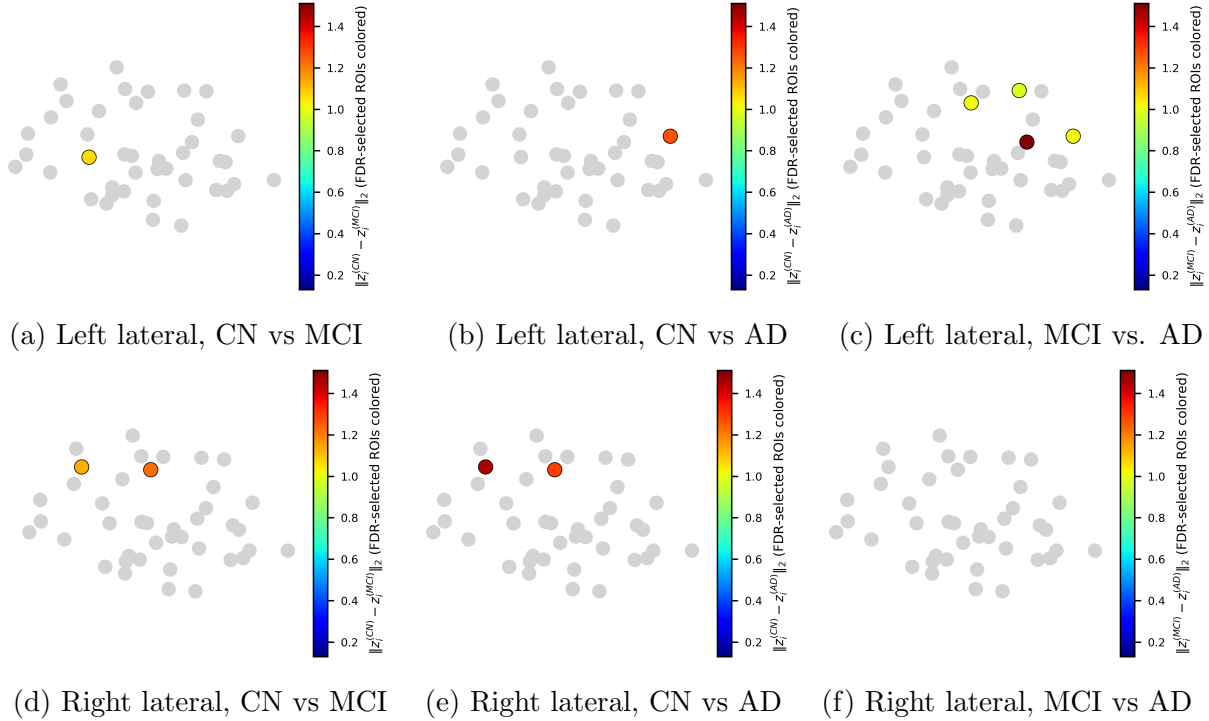


Figure 10: Lateral views of ROI-wise differences in the latent positions. Left-lateral and right-lateral brain maps color the magnitude of the latent displacement $\|z_i^{(p)} - z_i^{(q)}\|_2$ between groups. The same color scale is used across panels.

B.7 Computational performance for model with both zero-dimensional and one-dimensional features

We conduct simulations involving both zero-dimensional and one-dimensional features. We first generate oracle points $n = 150$ on two circles, both centered at origin in \mathbb{R}^2 but with radii 1 and 2, respectively. We then generate 10 subjects of data by adding independent noise from $N(0, 0.05^2 I)$ to each point. We obtain the persistence barcode, and then fit our model to the data. Figure 11 shows the autocorrelation function for all elements of Λ . The computational performance is comparable to the one we demonstrate in the main text.

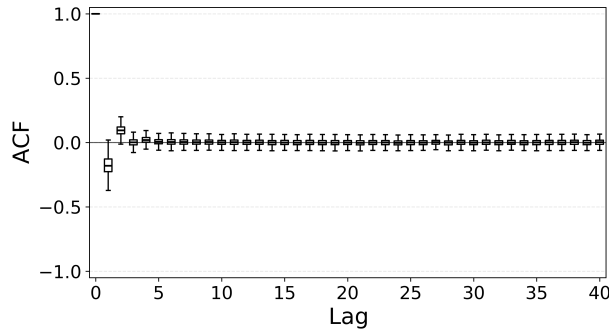


Figure 11: The boxplots of the autocorrelation function for all elements of Λ .